Journal of Materials Chemistry C

ROYAL SOCIETY OF CHEMISTRY

PAPER

View Article Online
View Journal | View Issue

Check for updates

Cite this: J. Mater. Chem. C, 2020, 8, 10791

Controlling the preferred orientation of layered BiOI solar absorbers†‡

Robert A. Jagt, * Tahmida N. Huq, Katharina M. Börsig, Daniella Sauven, Lana C. Lee, Judith L. MacManus-Driscoll and Robert L. Z. Hoye *§

Received 28th April 2020,
Accepted 11th June 2020

DOI: 10.1039/d0tc02076a

rsc.li/materials-c

Bismuth oxyiodide (BiOI) has gained attention for photovoltaics, photocatalysis and photodetectors owing to its composition of non-toxic elements, tolerance to point defects, and highly-suitable optical properties. But like many other bismuth-based compounds, BiOI is a layered material with anisotropic transport properties, making control over the preferred orientation critical for achieving optimal device performance. In this work, we develop new insights into the growth mechanism of BiOI synthesized by chemical vapor deposition (CVD) and show how the preferred orientation can be controlled. By adjusting the precursor and substrate temperatures to tune whether or not we are in a nucleation- or growth-controlled regime, we reproducibly vary the ratio of the (001) and (110) orientations by over two orders of magnitude. As a result, we achieve highly *c*-axis oriented films, which leads to less shunting than *a*/*b*-axis oriented films, resulting in improved open-circuit voltages from a median value of 0.7 V (*a*/*b*-axis oriented) to 0.9 V (*c*-axis oriented) in BiOI solar cells. More broadly, the described mechanisms can be used to control the preferred orientation in other low-dimensional materials, which will be important for achieving improved performance across a wide variety of devices.

Open Access Article. Published on 15 junio 2020. Downloaded on 07/11/2024 17:25:20.
This article is licensed under a Creative Commons Attribution 3.0 Unported Licence.

Introduction

Low-dimensional compounds have gained significant attention for a wide range of electronic applications. Popular examples of such compounds are two-dimensional materials, including graphene, hexagonal boron nitride and transition metal dichalcogenides.[1] These materials can be used for a variety of applications, including field-effect transistors,[2] light-emitting diodes,[3] photodetectors,[4] solar cells,[5] sensors,[6] catalytic reactors,[7] and single photon sources.[8] But low-dimensional bulk thin films have also been gaining increasing attention, particularly for photovoltaics. This has been driven by efforts to find Earth-abundant and non-toxic alternatives to cadmium telluride, copper indium gallium diselenide and lead-halide perovskite solar cells.[9–12] There has been particular focus on antimony- and bismuth-based materials because (i) these cations form a stable lone pair of valence electrons that hybridize with anion p orbitals to yield an electronic structure that may be conducive to shallow trap formation,[11] and (ii) most compounds have been found to be thermodynamically stable, unlike methylammonium lead iodide perovskites.[13,14] One example is bismuth oxyiodide (BiOI).

BiOI consists of layers of planes comprised of bismuth covalently bonded to iodine and oxygen (Fig. 1a). All elements are sufficiently abundant for commercialization and Bi-based compounds have demonstrated very little evidence of toxicity.[15,16] We have recently shown BiOI to tolerate vacancy and anti-site defects,[16,17] and found the unencapsulated films to be phase-stable in ambient air for >197 days.[16] With a band gap of 1.9 eV and absorption coefficient $>10^4$ cm^{-1}, BiOI has suitable optical properties for photovoltaics, indoor solar cells, photocatalysis[18–21] and photodetectors.[22,23] However, the transport properties are highly anisotropic. Within each I–Bi–O–Bi–I plane, there are low carrier effective masses. However, between planes, effective masses are high and carrier mobilities low.[24] Thus, in vertical-structured devices (*e.g.*, photovoltaics), it is essential to orient the grains to connect the top and bottom electrodes with the higher-mobility planes. Previously, we were able to achieve this by growing BiOI on solution-processed nickel oxide. This led to (102) preferred orientation, and the covalently-bonded planes in BiOI ran between both electrodes. The devices had external quantum efficiencies (EQEs) up to 80% at 450 nm wavelength, which was among the highest EQEs for perovskite-inspired materials at the time of publication.[16] However, the open-circuit voltage (V_{OC}) was 0.75 V,[16] well below the V_{OC} limit of 1.34 V (refer to Section S2 of the ESI‡). The low V_{OC}, in part, arose from a low shunt resistance, which may have resulted from the open structure of the (102)-oriented BiOI.

From the Wulf construction it follows that BiOI grains grow as platelets.[25] Previous research has resulted in a wide variety of microstructures, including single crystalline flakes,[26] microspheres

Department of Materials Science and Metallurgy, University of Cambridge, 27 Charles Babbage Road, Cambridge CB3 0FS, UK. E-mail: raj52@cam.ac.uk

† The raw data is available from DOI: 10.14469/hpc/7248.

‡ Electronic supplementary information (ESI) available. See DOI: 10.1039/d0tc02076a

§ Present address: Department of Materials, Imperial College London, Exhibition Road, London SW7 2AZ, UK. Email: r.hoye@imperial.ac.uk

Open Access Article. Published on 15 junio 2020. Downloaded on 07/11/2024 17:25:20.
This article is licensed under a Creative Commons Attribution 3.0 Unported Licence.

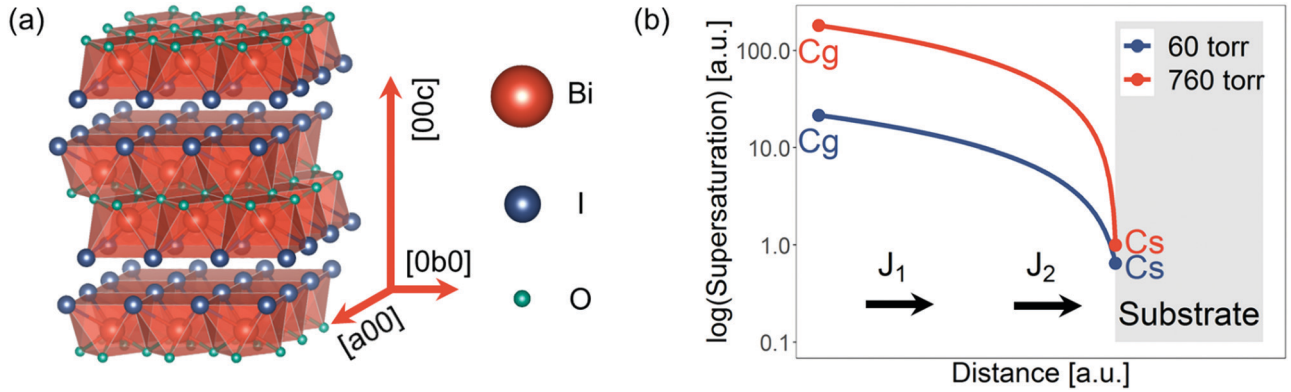

Fig. 1 (a) Crystal structure of bismuth oxyiodide with the axes given. (b) Schematic representation of how the supersaturation (concentration of active species in the gas phase in excess of the equilibrium concentration) changes as a function of the distance to the substrate across the boundary layer at 760 Torr (red) and 60 Torr (blue).

consisting of nanoplatelets,[27] thin films with varying preferred orientation,[18] and epitaxially grown BiOI onto MgO.[28] Like other layered material systems, this anisotropic growth poses significant challenges for device fabrication and careful control of the processing conditions is needed to maximize device performance. However, a systematic study of how the preferred orientation is dependent on processing conditions is lacking in BiOI, as well as in many other low-dimensional systems. Under thermodynamically-governed conditions, grains with no dangling bonds on the surface preferentially form in order to minimize the surface energy. This would therefore favor the *c*-axis orientation because the surfaces terminating along the [001] direction, unlike other crystallographic directions, leave no dangling bonds behind. Previous work on two-dimensional MoS_2 and $MoSe_2$, as well as one-dimensional Sb_2Se_3, showed that the thermodynamically-favored orientation could be overcome to achieve an *a*-axis orientation through a high growth rate, which could be controlled through the substrate temperature.[10,29] However, the final film microstructure is also dependent on many other experimental parameters, such as the supersaturation of the active species, orientation of the seed layer, and pressure, among others.[30–33] Understanding the role these parameters play will be important to fully control the preferred orientation of BiOI thin films.

In this work, we study the growth kinetics and determine the parameters that control the preferred orientation of BiOI thin films grown by chemical vapor deposition (CVD). Through detailed X-ray diffraction (XRD) measurements, we determine how these parameters influence the preferred orientation and obtain detailed insights into the growth mechanisms. By varying the preferred orientation of the BiOI thin films by two orders of magnitude, we demonstrate the effects of *c*-axis oriented films compared to *a*/*b*-axis oriented films on solar cell performance.

Experimental section

BiOI was grown by chemical vapor deposition (CVD) inside a two-zone tube furnace utilizing BiI_3 (99.99% metals basis, Sigma Aldrich) as the precursor and an Ar/O_2 gas mixture (4.5 and 19 mL min^{-1} for O_2 and Ar respectively) to oxidize and transport the vaporized BiI_3. A schematic of the reactor and the chemical vapor deposition reaction process can be found in Fig. S1, ESI.‡ The crucible with BiI_3 precursor was placed close to zone 1 inside the two-zone tube furnace. Up to four glass/ITO substrates coated with ~15 nm thick NiO_x (see ref. 17 for spin-coating procedure) were placed several centimeters away from the crucible. The temperature of the crucible and substrates were controlled independently by changing the temperatures of zones 1 and 2 individually in the furnace. The entire temperature profile inside the furnace was measured and calibrated with a thermocouple prior to the start of the growth runs for each temperature setting. See Fig. S3, ESI‡ for a temperature calibration curve. For the solar cells, 25 nm ZnO was deposited on ITO/NiO_x/BiOI by atmospheric pressure chemical vapor deposition at 80 °C (refer to ref. 16 for experimental details). Cr (20 nm) and Ag (100 nm) were deposited as electrodes through thermal evaporation. The solar cells were measured under a solar simulator calibrated to AM 1.5G radiation using a procedure reported earlier.[34] For more details on the band structure, refer to ref. 16.

X-ray diffraction measurements were performed using a Bruker D8 theta/theta system. Cu Kα radiation (λ = 1.5406 Å) was used as the X-ray source. All scanning electron microscopy images were taken on a FEI Nova NanoSEM. The film thickness was measured by scratching part of the film off and tracing the step-edge with a Dektak profilometer.[35]

Results and discussion

CVD-grown BiOI is formed by the reaction of evaporated BiI_3 with O_2 through the following reaction

$$BiI_3 + \frac{1}{2}O_2 \rightarrow BiOI + I_2 \quad (1)$$

There are several factors influencing the final microstructure of the films and there are several experimental conditions which can be changed to (indirectly) control these. The BiI_3 precursor sublimes from the crucible and is transported to the substrates with the aid of a carrier gas. The precursor diffuses through a

 This journal is © The Royal Society of Chemistry 2020

Open Access Article. Published on 15 junio 2020. Downloaded on 07/11/2024 17:25:20.
This article is licensed under a Creative Commons Attribution 3.0 Unported Licence.

boundary layer towards the surface of the substrate (in this case, NiO_x-coated glass) where it is adsorbed, decomposes and reacts to form a film. The by-products diffuse away and are extracted. For a schematic of this process see Fig. S1b with further details in Fig. S2, ESI.‡

Two main transport processes govern the growth kinetics: (1) mass transport of the active species through the boundary layer to the surface, and (2) reaction of the active species on the substrate. The concentration of the reactants on the substrate (defined as C_s) is lower than the concentration of the reactants in the carrier gas (defined as C_g), because the surface reaction depletes it. The flux density of active species, J_1, through the boundary layer can be written as

$$J_1 = h_g(C_g - C_s), \quad (2)$$

where $h_g \propto \frac{T_{sub}{}^{3/2}}{P}$, T_{sub} is the substrate temperature and P is the pressure. We note that the concentration of the gas species is proportional to the pressure, according to the ideal gas law. Thus, J_1 would not significantly depend on pressure but is temperature-dependent.

The flux density of active species consumed in the reaction, J_2, can be written as

$$J_2 = k_s C_s, \quad (3)$$

where $k_s \propto \exp\left(\frac{-E_a}{kT_{sub}}\right)$ and E_a is the activation energy for the reaction. Thus, J_2 is temperature-dependent, but also pressure-dependent, since C_s is proportional to the pressure.

In equilibrium, these two flux densities need to be balanced, *i.e.*, $J_1 = J_2$.

There are now two distinctive regimes, namely transport-limited growth (when $h_g \ll k_s$) and reaction-limited growth (when $k_s \ll h_g$). For transport-limited growth, the concentration of the reactants on the substrate surface is much smaller than in the gas phase ($C_s \ll C_g$), whereas for reaction-limited growth the two concentrations are nearly equal ($C_s \approx C_g$). From eqn (2) and (3), it can be seen the growth regime is determined by the substrate temperature and pressure. However, the nucleation rate is affected by the supersaturation (concentration of the active species above the equilibrium concentration). A schematic of how the supersaturation of the species depends on the distance from the substrate across the boundary layer is depicted in Fig. 1b. The supersaturation can be controlled through the temperature of the BiI_3 precursor (T_p). We note that the surface energy of the substrate, distance between precursor and substrate, and gas flow rate also influence growth. But in this work, we focus on the precursor and substrate temperatures, growth time, as well as the pressure, which we can independently and reproducibly control.

The measured X-ray diffraction pattern of the BiOI thin films grown for different times, growth temperatures and pressures are shown in Fig. 2. For Fig. 2a, we kept the precursor temperature at 320 °C, substrate temperature at 360 °C and the pressure at atmospheric pressure. We found the films to initially have no preferred orientation. But progressively, the

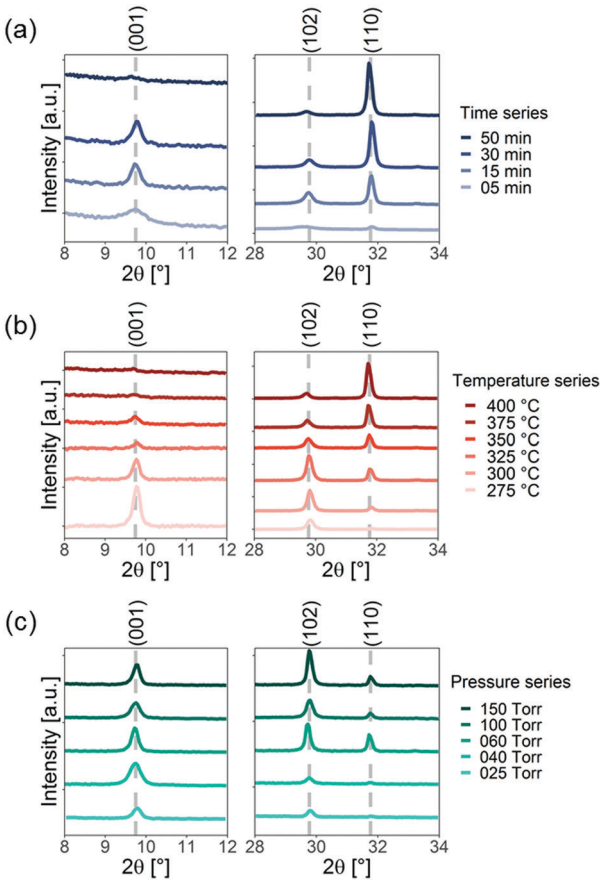

Fig. 2 X-ray diffraction pattern of bismuth oxyiodide grown by chemical vapor deposition (a) during different growth times, (b) at different growth temperatures (where $T_{sub} = T_p + 30$ °C) and (c) different growth pressures. Note that the scales of the vertical axes are different for visualization purposes. The full XRD patterns can be found in Fig. S5, ESI.‡

(110) peak became more dominant until the films were preferentially *a*/*b*-axis oriented after 50 min of growth (Fig. 2a). However, we found that the final orientation depends on the growth temperature (Fig. 2b). In Fig. 2b, we kept the substrate temperature at 30 °C above the precursor temperature, and adjusted the growth time to account for changes in the growth rate to keep the film thickness equal to approximately 700 nm. We examine the effect of the substrate temperature in more detail below. By contrast, the pressure did not have as strong an influence on the preferred orientation. In Fig. 2c, we kept the precursor temperature at 325 °C, and substrate temperature at 360 °C, and maintained a growth time of 30 min. At low pressure (25 Torr), the films had a slight *c*-axis preferred orientation. This only changed marginally when the pressure was increased from 25 Torr to 150 Torr.

To understand the role each of these parameters plays on preferred orientation, we systematically analyzed the growth rate and how the preferred orientation changes. This is shown in Fig. 3. We describe the preferred orientation from the ratio of the intensity of the (001) diffraction peak to the (110) diffraction peak after subtracting the background. This (001)/(110) intensity ratio is then multiplied by the (110)/(001) intensity ratio

Open Access Article. Published on 15 junio 2020. Downloaded on 07/11/2024 17:25:20.
This article is licensed under a Creative Commons Attribution 3.0 Unported Licence.

obtained from a powder sample (JCPDS No. 10-0445, I_{110} = 423, I_{001} = 398, I_{102} = 1000), which does not have preferred orientation. We refer to the product between these two ratios as the scaled (001)/(110) intensity ratio. A scaled intensity ratio of 1 implies that there is no preferred orientation. We first discuss the experimental results presented in Fig. 3 before discussing the growth mechanism.

We measured the growth rate as a function of the temperature at 60 Torr and 760 Torr pressure (Fig. 3a). We found only a slight increase in growth rate when the pressure was increased. For reaction-limited growth (where $C_s \approx C_g$) the growth rate should drop by more than an order of magnitude if the pressure is reduced by more than an order of magnitude, due to changes in the concentration of species in the gas phase with pressure. For transport-limited growth, one would expect pressure to have little effect on the growth rate (see eqn (2)). This is because although the concentration of reactants in the gas phase decreases by an order of magnitude, the diffusivity increases by more than an order of magnitude due to the increased mean free path of the gaseous species. Our results therefore imply that the growth of BiOI by CVD at atmospheric pressure is governed mainly by the transport-limited regime (*i.e.*, limited by J_1) as is expected.[30]

We observed the growth rate to have an exponential relationship to the inverse of temperature (Fig. 3a), showing there to be an activation energy barrier. We found that the extracted activation energy barriers (100 ± 10 kJ mol^{-1} and 80 ± 20 kJ mol^{-1} at 60 Torr and 760 Torr pressure respectively) were both close to the sublimation enthalpy of BiI_3 (125 kJ mol^{-1}).[36] This suggests that the growth rate was mostly determined by the supersaturation of the BiI_3 precursor in the gas phase.

The role of substrate temperature on the scaled (001)/(110) intensity ratio is shown in Fig. 3b. It can be seen that across different precursor temperatures, increasing the substrate temperature resulted in a strong decrease in the scaled (001)/(110) intensity ratio. This shows that the films are *c*-axis oriented at low substrate temperatures, becoming *a*/*b*-axis oriented at higher substrate temperatures. By varying the substrate temperature from 275 °C to 400 °C, the scaled (001)/(110) intensity ratio changed by two orders of magnitude. Thus, increasing the substrate temperature favored *a*/*b*-axis oriented platelets.

Next we focused on understanding how the preferred orientation develops over time. We measured the diffraction patterns of the films grown for different times. The precursor temperature was kept constant to 320 °C to maintain a constant supersaturation of the active species, and we measured the scaled intensity ratio for two substrate temperatures, T_{sub} = 280 °C and T_{sub} = 360 °C. At short growth times, films from both series had no preferred orientation. This indicates that for these films, the

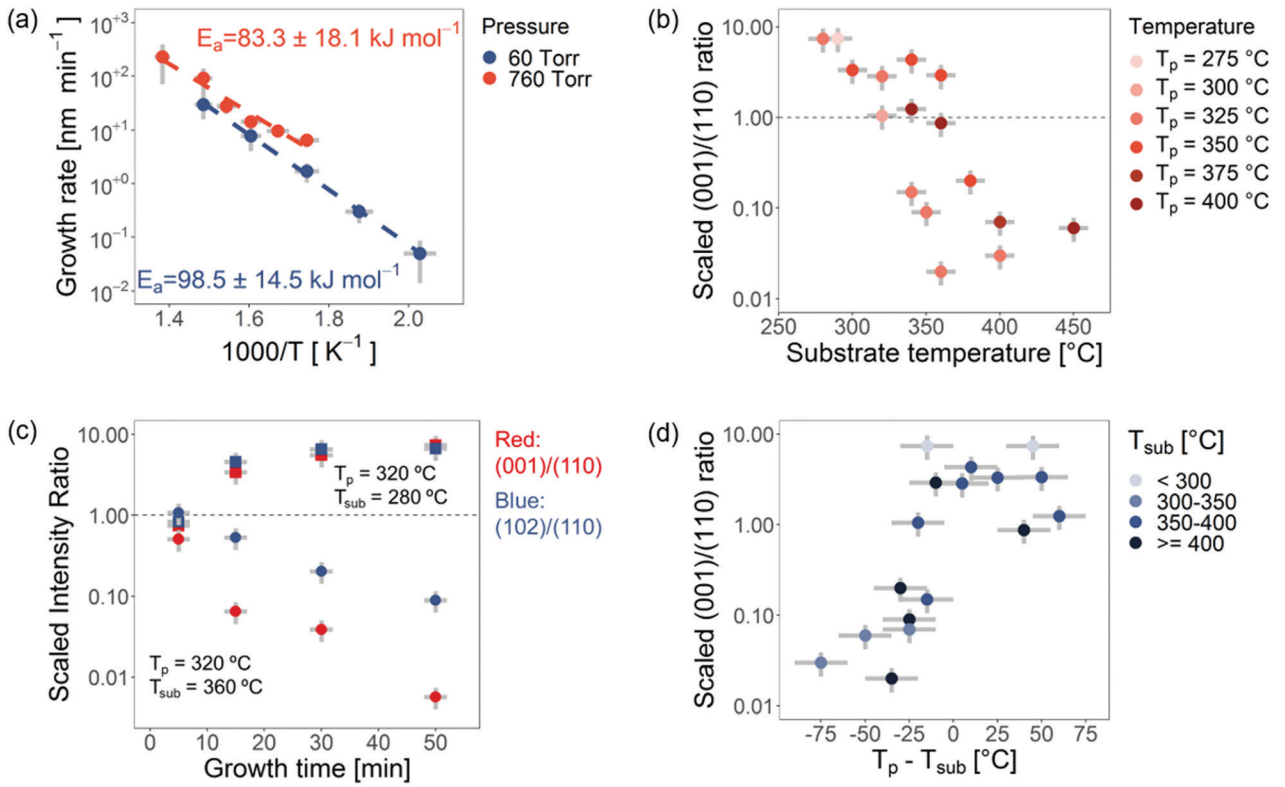

Fig. 3 Effect of the precursor (T_p) and substrate (T_{sub}) temperatures, pressure and growth time on the preferred orientation of BiOI thin films grown on glass coated with solution-processed NiO_x. (a) Growth rate as a function of precursor temperature measured at 60 Torr and 760 Torr. (b) Scaled (001)/(110) intensity ratio as a function of substrate temperature for films grown with different precursor temperatures. (c) Change in the preferred orientation as a function of growth time. The colors indicate the ratio of the (001) and (110) diffraction peaks (red), and of the (102) and (110) peaks (blue). The shapes indicate different substrate temperatures. Both series of films are grown with a precursor temperature of 320 °C. (d) Scatter plot of the scaled (001)/(110) intensity ratio against the difference between the precursor and substrate temperatures. The color scale indicates the range of substrate temperatures.

 This journal is © The Royal Society of Chemistry 2020

Open Access Article. Published on 15 junio 2020. Downloaded on 07/11/2024 17:25:20.
This article is licensed under a Creative Commons Attribution 3.0 Unported Licence.

interface energy between the (001) and (110) planes in BiOI and the solution-processed NiO_x are similar, and that there is no preferred nucleation of one orientation over the other. By contrast, BiOI grown onto single-crystalline MgO or Mica substrates has a predominantly *c*-axis orientation due to a lower interface energy between the substrate and the (001) BiOI plane.[22,28] Similarly in Sb_2Se_3 and 2D perovskites it has been found that the preferred orientation depends on the seed layer.[33,37] The preferred orientation of the BiOI films grown on NiO_x-coated glass is developed over the course of the growth period, with the films grown with a lower substrate temperature developing a *c*-axis orientation, while the films with the higher substrate temperature developed an *a*/*b*-axis orientation (Fig. 3c).

Lastly in Fig. 3d, the scaled (001)/(110) intensity ratio is depicted as a function of the difference between the precursor and substrate temperatures. It is clear that this ratio tends to increase as the temperature difference increases, and with no temperature difference resulting in the scaled (001)/(110) intensity ratio scattered about unity. In addition, this shows that increasing the precursor temperature relative to the substrate temperature results in more *c*-axis oriented films (and *vice versa* when the precursor temperature is decreased relative to the substrate temperature).

By combining all of the data in Fig. 2 and 3, it is possible to deduce the growth mechanism that gives rise to the changes in preferred orientation. Here we define two growth regimes: (1) nucleation-dominated and (2) grain growth-dominated. The first regime is obtained at high supersaturation (giving rise to a high nucleation rate). The nucleation-dominated regime generates predominately *c*-axis oriented films, because growing grains with a *c*-axis orientation requires the nucleation of a new layer on top of the existing grain. This occurs for high precursor temperatures, which would result in a higher concentration of the active species in the gas phase (higher supersaturation) and is in agreement with the observations in Fig. 3d. By contrast, the grain growth-dominated regime is favored when the substrate temperature is higher (especially when it is higher than the precursor temperature). For grains with *a*/*b*-axis orientation the grains terminate with surface dangling bonds. Growth of these grains requires the growth of the existing grain, which is mostly determined by the substrate temperature. Thus, from Fig. 3c and d we conclude that films start with no preferred orientation, but one orientation then outgrows the other as growth progresses and depends on whether we are in a nucleation dominated or grain growth dominated regime. Interestingly, the observed preferred orientation is not just a function of the growth rate. When the precursor temperature is sufficiently larger than the substrate temperature the films become predominantly *c*-axis oriented despite high growth rates. For example, it was possible to obtain films with *c*-axis preferred orientation, despite being grown at a high growth

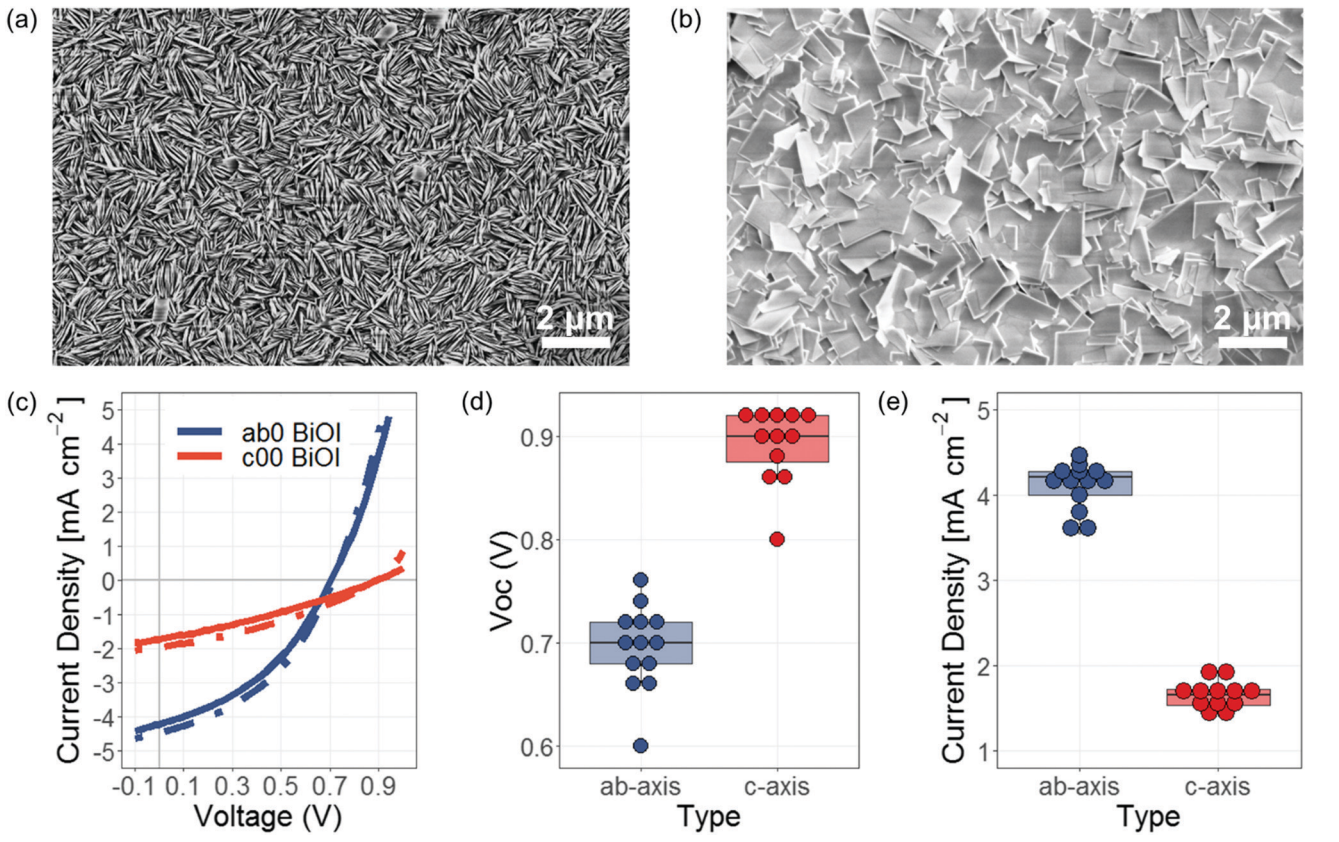

Fig. 4 Scanning electron microscopy image of (a) predominantly *a*/*b*-axis oriented films and (b) predominantly *c*-axis oriented films. (c) Representative current density *vs.* voltage measurements of *a*/*b*-axis (blue) and *c*-axis (red) oriented BiOI films in devices. The solid line is from the forward sweep and dashed line from the reverse sweep. Histogram of the (d) open circuit voltage (V_{OC}) and (e) short-circuit current density (J_{SC}) of 12–13 devices with the *a*/*b*-axis (blue) and *c*-axis (red) orientations.

Open Access Article. Published on 15 junio 2020. Downloaded on 07/11/2024 17:25:20.
This article is licensed under a Creative Commons Attribution 3.0 Unported Licence.

rate of 24.6 nm min^{-1}, by having T_p (400 °C) larger than T_{sub} (340 °C). We emphasize that the final orientation of the thin film is not just a function of the difference between the precursor and substrate temperatures. As depicted in Fig. 2b and 3b, d, for a given difference between the precursor and substrate temperature, the films tend to become more *a*/*b*-axis oriented for higher substrate temperatures. This is because higher substrate temperatures lead to the grain-growth dominated regime being favored.

To illustrate a potential benefit of being able to control the preferred orientation of BiOI, we investigated its effect on solar cell performance. The device structure was (150 nm) ITO|(15 nm) NiO_x| (750 nm) BiOI|(25 nm) ZnO|(20 nm) Cr|(100 nm) Ag. We used BiOI grown with T_p = 275 °C and T_{sub} = 290 °C (giving *c*-axis oriented platelets), and T_p = 325 °C and T_{sub} = 360 °C (giving *a*/*b*-axis oriented platelets). Note that for the *c*-axis oriented film, the substrate temperature is above the precursor temperature, but due to the small temperature difference and low substrate temperature, a *c*-axis preferred orientation was obtained (see Fig. 2b and 3d). The morphology of these films is given in Fig. 4a and b. From the scanning electron microscopy images, it can be seen that the *c*-axis oriented films have a significantly more compact structure, with fewer shunt pathways available. Two representative current density *vs.* voltage (*I*–*V*) curves for devices made from films with both orientations are shown together with two boxplots for the V_{OC} and short-circuit current density (J_{SC}) in Fig. 4c–e. The V_{OC} was significantly improved from a median of 0.7 V (0.78 V maximum) to a median of 0.9 V (0.93 V maximum). The improved V_{OC} was due to an increase in the shunt resistance from 470 ± 70 Ω cm^2 to 850 ± 210 Ω cm^2 (see also Fig. S6, ESI‡). This is closer to the V_{OC} limit of 1.34 V, which was calculated using methods reported in ref. 38 and accounts for the Urbach energy of the system. The improved V_{OC} is now comparable to amorphous silicon and other organic systems with similar Urbach energies and band gaps as BiOI.[38] That is, by 'closing-up' the morphology of BiOI through a *c*-axis preferred orientation, we were able to achieve comparable V_{OC}s as three-dimensional systems that do not have the same anisotropy challenges as BiOI.

However, the limitation of making a solar cell with a *c*-axis oriented layered material is that the top and bottom electrodes are not connected with the higher-mobility planes. As a result, the J_{SC} was lower for the *c*-axis oriented film compared to the *a*/*b*-axis oriented film (Fig. 4c and e). Similar results have been found in other low-dimensional systems.[33,39] Future improvements in performance may require a combination of *a*/*b*-axis and *c*-axis oriented platelets. Alternatively, a back contact structure may be explored using *c*-axis oriented BiOI.[40] Beyond photovoltaics, *c*-axis oriented BiOI with dense morphology would also be suitable for field effect transistors.[41] Nevertheless, we show the potential of BiOI if the challenges due to shunting are overcome. We also note that the calculated V_{OC} limit of 1.34 V is lower than the radiative limit for a 1.9 eV band gap semiconductor (1.6 V).[42] Further improvements in performance would also require improving the quality of BiOI grown to reduce the Urbach energy from 40–70 meV (depending on the growth temperature) to below 30 meV.

Conclusions

In this work we have identified the growth mechanism of CVD-grown BiOI. Contrary to previous work on growing *a*-axis oriented low-dimensional materials, we show that the preferred orientation of BiOI depends on the interplay between nucleation and growth, and not solely on the growth rate. By varying the substrate and precursor temperatures, the growth regime for BiOI can be tuned from nucleation-dominated to grain growth-dominated. By changing the substrate temperature and the difference between the precursor and substrate temperatures, the preferred orientation can be changed from *c*-axis oriented to *a*/*b*-axis oriented, and the scaled (001)/(110) intensity ratio can be changed over two orders of magnitude. We also show that the growth pressure has a smaller effect on preferred orientation, owing to the fact that the growth is mass transport limited rather than surface reaction limited. Through our new understanding of the mechanism of CVD BiOI growth, we were able to achieve highly *c*-axis oriented BiOI films, with a more compact morphology than our previous *a*/*b*-axis oriented films. This resulted in the V_{OC} improving from a median of 0.7 V to 0.9 V (0.93 V maximum), showing both the potential of addressing morphology-related shunting issues in this system, as well as the future work needed to further improve this system, such as reducing the Urbach energy. Our work can be more broadly applied across other low-dimensional systems to provide a systematic way to control the experimental parameters that most influence the preferred orientation, which has a strong influence on device performance.

Author contributions

R. A. J. conceived of the idea behind the project. R. A. J., T. N. H., K. M. B., D. S., L. C. L. grew the BiOI films, measured the morphology and measured the diffraction patterns. R. A. J. and T. N. H. made and tested the solar cells. R. L. Z. H. supervised the work, along with J. L. M.-D. All authors contributed to analyzing the data and writing the text.

Conflicts of interest

There are no conflicts to declare.

Acknowledgements

R. A. J. acknowledges funding from an EPSRC Department Training Partnership studentship (No. EP/N509620/1), as well as Bill Welland and the Winton Programme for the Physics of Sustainability. T. N. H. acknowledges funding from the EPSRC Centre for Doctoral Training in Graphene Technology (No. EP/L016087/1) and the Aziz Foundation. L. C. L. acknowledges funding from the EPSRC Centre for Doctoral Training in New and Sustainable Photovoltaics. J. L. M.-D. acknowledges funding from the Royal Academy of Engineering under the Chair in Emerging Technologies Scheme (No. CIET1819_24). R. L. Z. H. acknowledges funding from the Royal Academy of Engineering

 This journal is © The Royal Society of Chemistry 2020

under the Research Fellowship scheme (No. RF\201718\1701), Downing College Cambridge (Kim and Juliana Silverman Research Fellowship), and the Isaac Newton Trust (Minute 19.07(d)).

Open Access Article. Published on 15 junio 2020. Downloaded on 07/11/2024 17:25:20.
This article is licensed under a Creative Commons Attribution 3.0 Unported Licence.

References

1 A. C. Ferrari, M. Katsnelson, L. Vandersypen, A. Loiseau, V. Morandi, A. Tredicucci, G. M. Williams and H. Hong, *Nanoscale*, 2015, **7**, 4598–4810.
2 B. Radisavljevic, A. Radenovic, J. Brivio, V. Giacometti and A. Kis, *Nat. Nanotechnol.*, 2011, **6**, 147–150.
3 Z. Wang, Q. Jingjing, X. Wang, Z. Zhang, Y. Chen, X. Huang and W. Huang, *Chem. Soc. Rev.*, 2018, **16**, 6128–6174.
4 G. Wang, Y. Zhang, C. You, B. Liu and Y. Yang, *Infrared Phys. Technol.*, 2018, **88**, 149–173.
5 O. S. Hutter, L. J. Phillips, K. Durose and J. D. Major, *Sol. Energy Mater. Sol. Cells*, 2018, **188**, 177–181.
6 D. Tyagi, H. Wang and W. Huang, *Nanoscale*, 2020, **12**, 3535–3559.
7 J. Deng, H. Li, J. Xiao, Y. Tu, D. Deng, H. Yang, H. Tian, J. Li, P. Ren and X. Bao, *Energy Environ. Sci.*, 2015, **8**, 1594–1601.
8 J. Wrachtrup, *Nat. Nanotechnol.*, 2016, **11**, 11–12.
9 Z. Li, X. Liang, G. Li, H. Liu, H. Zhang, J. Guo, J. Chen, K. Shen, X. San, W. Yu, R. E. I. Schropp and Y. Mai, *Nat. Commun.*, 2019, **10**, 125.
10 Y. Zhou, L. Wang, S. Chen, S. Qin, X. Liu, J. Chen, D. Xue, M. Luo, Y. Cao, Y. Cheng, E. H. Sargent and J. Tang, *Nat. Photonics*, 2015, **9**, 409–415.
11 R. E. Brandt, J. R. Poindexter, P. Gorai, R. C. Kurchin, R. L. Z. Hoye, L. Nienhaus, M. W. B. Wilson, J. A. Polizzotti, R. Sereika, Z. Raimundas, L. C. Lee, J. L. MacManus-Driscoll, M. Bawendi, V. Stevanović and T. Buonassisi, *Chem. Mater.*, 2017, **29**, 4667–4674.
12 M. Wang, H. Wang, W. Li, X. Hu, K. Sun and Z. Zang, *J. Mater. Chem. A*, 2019, **7**, 26421–26428.
13 W. Ke and M. G. Kanatzidis, *Nat. Commun.*, 2019, **10**, 965.
14 L. C. Lee, T. N. Huq, J. L. MacManus-Driscoll and R. L. Z. Hoye, *APL Mater.*, 2018, **6**, 084502.
15 R. Mohan, *Nat. Chem.*, 2010, **2**, 336.
16 R. L. Z. Hoye, L. C. Lee, R. C. Kurchin, T. N. Huq, K. H. L. Zhang, M. Sponseller, L. Nienhaus, R. E. Brandt, J. Jean, J. A. Polizzotti, A. Kursumović, M. G. Bawendi, V. Bulović, V. Stevanović, T. Buonassisi and J. L. MacManus-Driscoll, *Adv. Mater.*, 2017, **29**, 1702176.
17 T. N. Huq, L. C. Lee, L. Eyre, W. Li, R. A. Jagt, C. Kim, S. Fearn, V. Pecunia, F. Deschler, J. L. MacManus-Driscoll and R. L. Z. Hoye, *Adv. Funct. Mater.*, 2020, **30**, 1909983.
18 R. He, J. Zhang, J. Yu and S. Cao, *J. Colloid Interface Sci.*, 2016, **478**, 201–208.
19 L. Ye, J. Chen, L. Tian, J. Liu, T. Peng, K. Deng and L. Zan, *Appl. Catal., B*, 2013, **31**, 8978–8983.
20 J. Li, L. Zhang and Y. Yu, *Nanoscale*, 2014, **6**, 8473–8488.
21 H. Li, Z. Yang, J. Zhang, Y. Huang, H. Ji and Y. Tong, *Appl. Surf. Sci.*, 2017, **423**, 1188–1197.
22 W. Zeng, J. Li, L. Feng, H. Pan, X. Zhang, H. Sun and Z. Liu, *Adv. Funct. Mater.*, 2019, **29**, 1900129.
23 M. D. Prasad, M. G. Krishna and S. K. Batabyal, *ACS Appl. Nano Mater.*, 2019, **2**, 3906–3915.
24 A. M. Ganose, M. Cu, K. T. Butler, A. Walsh and D. O. Scanlon, *Chem. Mater.*, 2016, **28**, 1980–1984.
25 M. V. Laue, *Z. Kristallogr. Cryst. Mater.*, 1943, **105**, 124–133.
26 H. Oppermann, M. Schmidt and P. Schmidt, *Z. Anorg. Allg. Chem.*, 2005, **631**, 197–238.
27 X. Zhang, Z. Ai, F. Jia and L. Zhang, *J. Phys. Chem. C*, 2008, **112**, 747–753.
28 M. Schuisky and A. Hârsta, *J. Electrochem. Soc.*, 1998, **145**, 4234–4239.
29 D. Kong, H. Wang, J. J. Cha, M. Pasta, K. J. Koski, J. Yao and Y. Cui, *Nano Lett.*, 2013, **13**, 1341–1347.
30 M. Oring, *The Material Science of Thin Films*, Elsevier, 2nd edn, 2002.
31 J. Zhou, J. Lin, X. Huang, Y. Zhou, Y. Chen, J. Xia, H. Wang, Y. Xie, H. Yu, J. Lei, D. Wu, F. Liu, Q. Fu, Q. Zeng, C. Hsu, C. Yang, L. Lu and T. Yu, *Nature*, 2018, **556**, 355–359.
32 X. Wen, C. Chen, S. Lu, K. Li, R. Kondrotas, Y. Zhao, W. Chen, L. Gao, C. Wang, J. Zhang, G. Niu and J. Tang, *Nat. Commun.*, 2018, **9**, 2179.
33 K. Li, C. Chen, S. Lu, C. Wang, S. Wang and Y. Lu, *Adv. Mater.*, 2019, **31**, 1903914.
34 R. D. Raninga, R. A. Jagt, S. Béchu, T. N. Huq, M. Nikolka, Y.-H. Lin, M. Sun, Z. Li, W. Li, M. Bouttemy, M. Frégnaux, H. J. Snaith, P. Schulz, J. L. MacManus-Driscoll and R. L. Z. Hoye, *Nano Energy*, 2020, 104946, DOI: 10.1016/j.nanoen.2020.104946.
35 R. A. Jagt, T. N. Huq, S. A. Hill, M. Thway, T. Liu, B. Roose, K. Gałkowsk, W. Li, S. F. Lin, D. Stranks, J. L. MacManus-Driscoll and R. L. Z. Hoye, 2020, arxiv 2001.07755.
36 J. H. Kim and S. Blairs, *J. Chem. Thermodyn.*, 1990, **22**, 803–814.
37 T. Liu, Y. Jiang, M. Qin, J. Liu, L. Sun, F. Qin, L. Hu, S. Xiong, X. Jiang, F. Jiang, P. Peng, S. Jin, X. Lu and Y. Zhou, *Nat. Commun.*, 2019, **10**, 878.
38 P. K. Nayak, S. Mahesh, H. J. Snaith and D. Cahen, *Nat. Rev. Mater.*, 2019, **4**, 269–285.
39 H. Tsai, W. Nie, J. Blancon, C. C. Stoumpos, R. Asadpour, B. Harutyunyan, A. J. Neukirch, R. Verduzco, J. J. Crochet, S. Tretiak, L. Pedesseau, J. Even, M. A. Alam, G. Gupta, J. Lou, P. M. Ajayan, M. J. Bedzyk, M. G. Kanatzidis and A. D. Mohite, *Nature*, 2016, **536**, 312–316.
40 G. D. Tainter, M. Luis, H. J. Joyce, G. D. Tainter, M. T. Ho and R. D. Lamboll, *Joule*, 2019, **3**, 1301–1313.
41 J. Wu, H. Yuan, M. Meng, C. Chen, Y. Sun, Z. Chen, W. Dang, C. Tan, Y. Liu, J. Yin, Y. Zhou, S. Huang, H. Q. Xu, Y. Cui, H. Y. Hwang, Z. Liu, Y. Chen, B. Yan and H. Peng, *Nat. Nanotechnol.*, 2017, **12**, 530–534.
42 A. Polman, M. Knight, E. C. Garnett, B. Ehrler and W. C. Sinke, *Science*, 2016, **352**, 307.